Proceedings of the ASME Fluids Engineering Division Summer Meeting
FEDSM2021
August 10-12, 2021, Virtual Conference, Online

FEDSM2021-62556

EXPERIMENTAL TESTING AND NUMERICAL MODELING OF SMALL-SCALE BOAT WITH DRAG-REDUCING AIR-CAVITY SYSTEM

Jeffrey M. Collins
Washington State University
Pullman, WA, USA

Phillip R. Whitworth
Washington State University
Pullman, WA, USA

Konstantin I. Matveev
Washington State University
Pullman, WA, USA

ABSTRACT

Hydrodynamic performance of ships can be greatly improved by the formation of air cavities under ship bottom with the purpose to decrease water friction on the hull surface. The air-cavity ships using this type of drag reduction are usually designed for and typically effective only in a relatively narrow range of speeds and hull attitudes and sufficient rates of air supply to the cavity. To investigate the behavior of a small-scale air-cavity boat operating under both favorable and detrimental loading and speed conditions, a remotely controlled model hull was equipped with a data acquisition system, video camera and onboard sensors to measure air-cavity characteristics, air supply rate and the boat speed, thrust and trim in operations on open-water reservoirs. These measurements were captured by a data logger and also wirelessly transmitted to a ground station and video monitor. The experimental air-cavity boat was tested in a range of speeds corresponding to length Froude numbers between 0.17 and 0.5 under three loading conditions, resulting in near zero trim and significant bow-up and bow-down trim angles at rest. Reduced cavity size and significantly increased drag occurred when operating at higher speeds, especially in the bow-up trim condition. The other objective of this study was to determine whether computational fluid dynamics simulations can adequately capture the recorded behavior of the boat and air cavity. A computational software Star-CCM+ was utilized with the VOF method employed for multi-phase flow, RANS approach for turbulence modeling, and economical mesh settings with refinements in the cavity region and near free surface. Upon conducting the mesh verification study, several experimental conditions were simulated, and approximate agreement with measured test data was found. Adaptive mesh refinement and time step controls were also applied to compare results with those obtained on the user-generated mesh. Adaptive controls improved resolution of complex shedding patterns from the air cavity but had little impact on overall results. The presented here experimental approach and obtained results indicate that both outdoor experimentation and computationally inexpensive modeling can be used in the process of developing air-cavity systems for ship hulls.

INTRODUCTION

The potential to reduce water drag on ships using various means of air lubrication on the underwater hull surface has long been known [1,2]. Commercial applications of air bubble injection (Figure 1a) have seen increasing deployment in recent years [3], often showing 5%-7% fuel savings under certain operating conditions. Air cavity drag reduction (Figure 1b) can potentially reduce a ship's propulsion energy consumption by 30% [4], although greater understanding of the air cavity physics is needed to achieve optimal performance and maintain drag saving effects across a range of operating conditions. In addition, applications of air cavities can reduce underwater noise emitted by a ship [5].

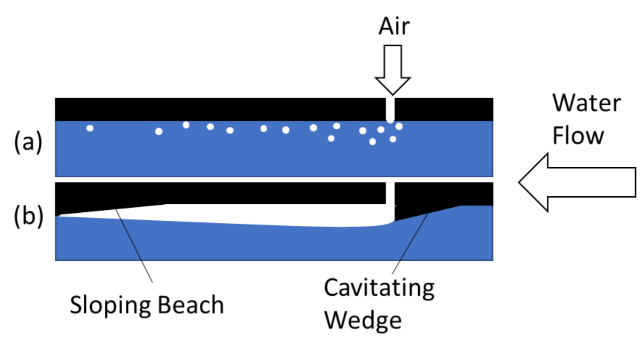

Figure 1. Bubble drag reduction (a), air cavity drag reduction (b). Air is shown in white.

Air lubrication can take several forms including continuous bubble injection (BDR), the formation of continuous air layers across flat regions of the hull (ALDR), and augmented air cavities formed inside of specially designed recesses in the hull surface (ACDR). Experiments performed on flat plates at high

Reynolds number have been well documented for BDR [6], ALDR [6] and some variations of ACDR [7,8]. BDR was shown to reduce friction locally by up to 20%, at which point increasing the air injection rate leads to the onset of ALDR [6]. Regions of the plate covered by the air layer showed local drag reduction over 95%, but the layer was thin and easily disrupted by disturbances in flow environment [6]. Adding geometric features to alter the incident water flow such as wedges near the injector [4,8,9] and sloping sections near the desired cavity closure point [7,10] to generate ACDR effects can create air cavities that are more stable and larger in volume than other methods. However, these features can increase form drag in non-ideal flow conditions and require further research into their effects on the general hydrodynamics of the ship to become commercially viable. In this study, an ACDR system has been implemented and explored on an experimental hull.

Results obtained in laboratory conditions with flat plates are helpful to establish general trends of the air cavity system, but are not sufficient guidelines for designing practical ships [11]. Experiments on more realistic hull shapes provide more insight into how the air cavity behaves in practical situations, particularly with changes in ship attitude. Air cavity models tested by Zverkhovskyi [10] showed that cavity behavior was extremely sensitive to heel effects, and the experimental setup was altered to stabilize heel angle of the model so that behavior of the air cavity could be studied more clearly. Experiments conducted by Hao et al. [12] found that air layer sizes on the model scale were severely diminished with heel angles of only 1°. Small-scale experiments in a water channel by Matveev et al. [13,14] demonstrated that air cavities achieve a maximum length with very small trim angles, but diminish very quickly with any trim beyond the optimal point. Experimental measurements of trim effects on the air-cavity hull performance is one of the aims of this study.

Due to lack of sufficient field data for air cavity ships to generate empirical correlations, modern computational fluid dynamics can be a useful tool for improving air cavity ship design. Early simulation efforts used data from previously described flat plate experiments as a validation case with limited success. In one study, air losses from the cavity were overpredicted by a factor of two [8]. Air cavity experiments performed by Shiri et al. [15] were accompanied by a CFD model which demonstrated that behavior of the air cavity, particularly in the closure region, could not be captured within a 2D simulation. More recent computational studies on the same experiment performed in 3D were able to accurately capture the cavity length and interface profile, while providing insight into the pressure distribution and air shedding mechanisms at the cavity closure regions [16]. Computational studies by Rotte et al. [17] have explored the validity of using Reynolds-averaged turbulence models with the volume-of-fluid interface capturing method and found that air shedding from the cavity can be predicted more accurately by limiting eddy viscosity in the turbulence model, and also by using methods that account for different size scales of turbulent motion.

Commercial air cavity ship design will require further simulation of coupling between the air cavity and ship motion. Experiments on a model air cavity planing yacht by Cucinotta et al. [18] were accompanied by CFD studies incorporating two degrees of freedom. Simulated results showed good agreement with the experiment for drag reduction and ship attitude, while air cavity shapes were qualitatively similar. For $Fr > 1$, the air cavity could not persist along some portions of the hull bottom, which was also predicted by the simulation. Experiments showing interactions between ship attitude and air cavity shapes performed by Hao et al. [12] were also successfully modelled using modern CFD software.

While these results are encouraging, more research is still required to develop general knowledge and confidence in computational methods for air-cavity hulls. Different flow conditions will likely require different modelling approaches for mesh generation, turbulence, and multi-phase interactions between the air, water, and solid hull. Additional experimental data are also needed to verify simulation results in a wide range of speed and loading conditions for different hull shapes. By measuring relevant cavity states under different hull loadings and water speeds, favorable operating conditions can be determined while detrimental states can be further studied to identify possible mitigation means, such as using adjustable actuators [12,19,20].

Most published experimental studies with air-cavity (and conventional) hulls have been carried out in towing tanks. While such tests are certainly more controlled and accurate than open-water experiments, testing in natural water reservoirs does not require large investments in experimental facilities and thus provides an attractive alternative for ship developers. A number of ship design bureaus and boating companies utilize open-water testing in their work [21]. Our group has built a variety of instrumented self-propelled models of marine and amphibious craft [22,23]. The present study aims to provide more insight into the performance of a model air cavity hull operated remotely on an open water surface, and to determine suitable CFD settings to capture important operating characteristics.

The boat hull used in this study was previously employed in open water experiments where speed and trim were measured as a function of thrust and demonstrated significant performance improvements between the air cavity and datum (solid) hull [24]. However, previous experiments lacked equipment for directly measuring characteristics of the air cavity and relied on analog instruments. Here, the model has been updated with a remote digital data acquisition systems and additional sensors to observe cavity length and pressure at different loading and speed conditions, providing more insight into cavity physics and a basis to validate computational models.

EXPERIMENTAL SETUP

The tested hull was constructed from Styrofoam coated with fiberglass, and the acrylic floor allows viewing of the cavity. Main dimensions and features of the hull are given in Figure 2. Geometry of the sloping beach was chosen to obtain smooth reattachment of the cavity to the recess ceiling at speeds below

1 m/s. Aluminum rails were installed around the deck for mounting motors and test equipment. Net weight of the system was 16.8 kg. A photograph of the test configuration is shown in Figure 3 (top). The outboard Dynamite A3650 2000Kv brushless motor was powered by a pair of 3S LiPo batteries connected to HobbyKing 120A electronic speed controller (ESC), with steering controlled by a servo arm as shown in Figure 3 (bottom).

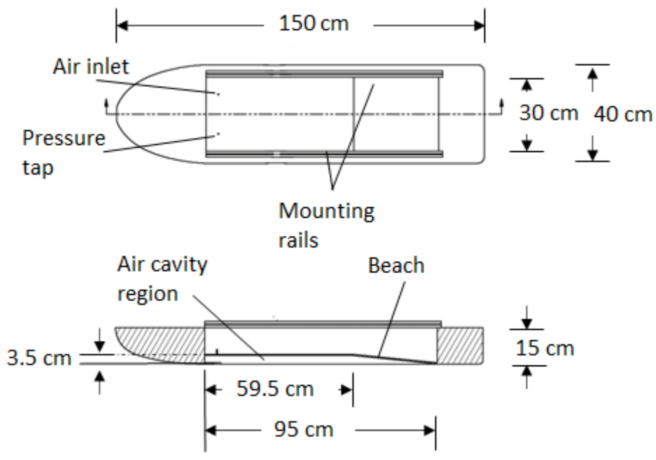

Figure 2. Main hull dimensions and features

Boat speed was measured using Adafruit ultimate breakout GPS module and trim by MPU-6050 accelerometer/gyroscope sensor. Component characteristics are listed in Table 1. Cavity pressure was monitored by a Honeywell SCXL004DN pressure transducer connected to an air tap located near the leading edge of the recess (see Figure 2). Airflow was supplied by a 12V DC pump and measured by the pressure drop across a constriction, which was calibrated using a rotameter before and after the test sequence. Inner diameter of the air inlet on the recess ceiling was 3 mm. Net thrust was measured using a CALT DYLY-103 load cell placed between the motor and hull. Load cell readings were deadweight tested through the custom-built DAQ system and subsequently field checked using an Omega DFG60-11 force sensor before each set of experiments. A first-person-view (FPV) camera was mounted above the acrylic floor to view cavity behavior during operation. Data was collected by an Arduino Mega 2560 R3 microcontroller at a rate of 10 Hz and radio-transmitted to a ground station for real-time monitoring.

Table 1. Range and accuracy of measuring instruments

Component	Range	Accuracy
Load cell (in situ)	0-100 N	± 0.3 N
Load cell (reference)	0-49 N	± 0.1 N
Pressure transducer	0-2000 Pa	± 20 Pa
Rotameter (reference)	0-40 sccs	± 1.0 sccs
Angle finder (reference)	0-90°	± 0.05°
Angle meter (in situ)	360°	± 0.12°

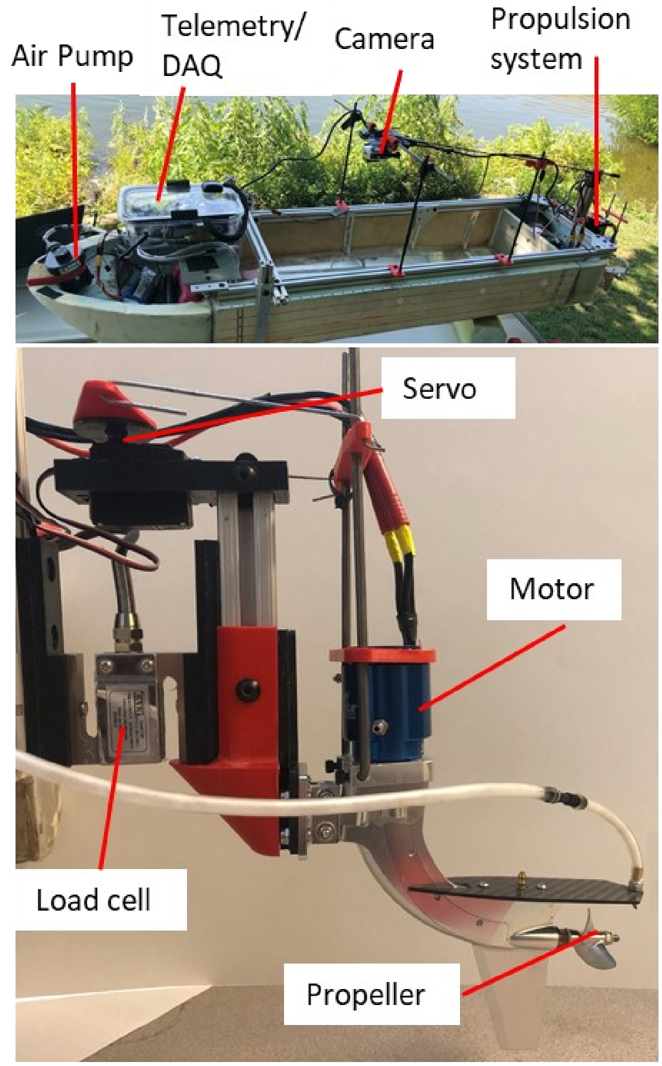

Figure 3. Photograph of tested configuration (top), close- up of propulsor and load cell (bottom)

A schematic of the electronic systems is shown in Figure 4. The schematic is separated into two main groups, onshore and onboard. The onshore systems aided in live data viewing which enabled remote tuning and control. Onboard systems include all main functions of the vessel and the manner in which they are interconnected. The data logger's main function was to read and condition the sensor measurements and then transmit the readings to the ground station and a storage device. ESC1 converted the remote-control signal into a DC voltage that drove the air pumps flow rate. ESC2 converted the remote-control signal into AC voltage to drive the brushless motor producing thrust. The developed experimental setup allowed measurement of important characteristics of a model air cavity boat operating in an open-water environment.

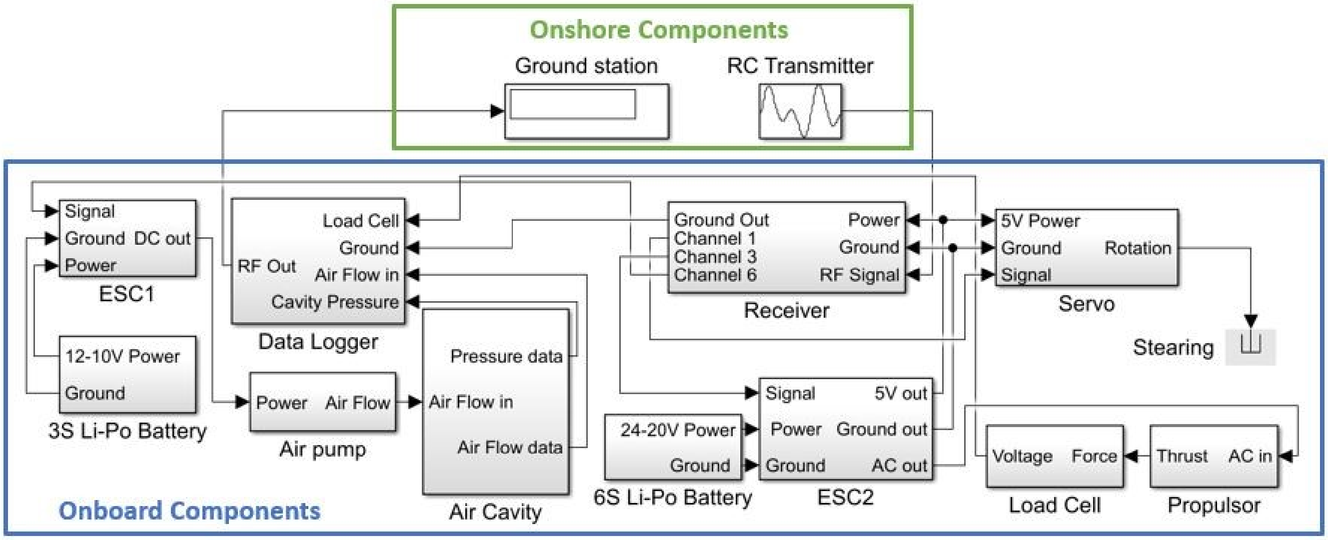

Figure 4. Schematic of vessel functions, remote control and data acquisition system

EXPERIMENTAL PROCEDURE

Testing was performed on a pond at Wawawai County Park near Pullman, Washington, during July and August of 2020. There was no noticeable wind on test days, and water elevation disturbances were below 1 cm. However, no measurements of environmental conditions were attempted. It should be noted that testing in open water with generally uncontrolled conditions is less accurate than laboratory tests, but it can expand ranges of studied parameters and provide a low-cost alternative to laboratory testing. Three different hull loadings were considered for this study, resulting in resting trim angles of -0.8°, 0°, and +0.8° without air injection.

Water speeds tested were between 0.6 m/s and 2.0 m/s, corresponding to a Reynolds number range of 1 to 3 million and a Froude number range of about 0.15-0.5 based on total hull length. For each data run, the air cavity was formed at rest and the hull was gently accelerated to the target speed. During tests, airflow to the cavity was held constant around 35 sccs. This flow rate was selected in initial tests to produce air cavities covering most of the bottom recess at low speeds, while keeping the nominal power for air supply below 2% of the propulsive power. Speed, trim, air supply rate, net thrust, and cavity pressure were recorded to the onboard data logger and monitored in real time from the ground station. Due to range limitations on data transmission, steady target speeds could only be maintained for time intervals between 4-8 s. After reaching the target speed, average cavity length was recorded based on visual inspection via FPV goggles.

Steady states were identified by time intervals of constant speed and thrust. Mean values from these intervals were reported as the primary data points. The random uncertainty, obtained from the standard deviation of each data set with t-values for a 95% confidence interval, was combined with the instrument uncertainty to determine the total experimental error. At high water speeds, run times were limited by the transmission range of DAQ signals. Hence, it is worth noting that cavity behavior recorded at these speeds may not represent the ideal steady state.

EXPERIMENTAL RESULTS

Experimental results for the tested conditions are shown in Figure 5. Normalized cavity length is reported as the measured length (L_c) in relation to the length of the recess region (L_r), which is equal to 95 cm (Figure 2). The non-dimensional air-cavity pressure can be expressed as the gage pressure (P_c) divided by the water column pressure of the step height ($\rho g h$). Froude number $Fr = U/\sqrt{gL}$, where U and L are the speed and hull length, is commonly used to characterize speed regimes.

For the front-loaded hull at low speeds, the ship maintained a negative trim. At this orientation, hydrostatic pressure decreased downstream along the cavity boundary, favoring air propagation toward the stern. This resulted in the greatest cavity length and lowest pressure among tested conditions, suggesting that the cavity thickness had been reduced at this speed and loading. Although cavity thickness was not directly observable in this setup, previous studies have also reported thinner cavities and increased air leakage with negative hull trim [13,14].

For the front-loading condition, increasing the speed to 1.34 m/s resulted in near-zero trim, which diminished cavity length by 15% but also increased pressure. Increasing the speed to 2.0 m/s caused an increase of trim to positive values, as well as a drop in both cavity length and pressure. Part of the reason for the cavity degradation was that positive hull trim caused an unfavorable hydrostatic pressure gradient that slowed downstream cavity growth and allowed water to impinge on the recess ceiling, resulting in a lower cavity length. The front portion of the cavity recess was slightly raised with positive hull trim, which decreased the average submergence depth and pressure in the cavity. Air losses from the cavity interface are also known to increase with turbulence [8], which may further explain the diminished cavity state at maximum speed.

For all loadings, hull trim increased very suddenly for speeds above 1.5 m/s. This correlates directly with increased drag and diminished cavity length. Total drag showed a much stronger correlation with trim than with cavity state, implying that the pressure component of the resistance was greater than the frictional drag. With extreme positive trim occurring at high speeds with the rear load condition, no stable cavity could be formed. In the absence of air coverage, the exposed beach inside of the cavity recess caused more form drag than would be expected from a smooth hull surface under the same conditions.

The experimental uncertainty in cavity length was due to primarily to large spacings between reference markers on the acrylic recess ceiling. Representative images of long and short cavities during operation are shown in Figure 6.

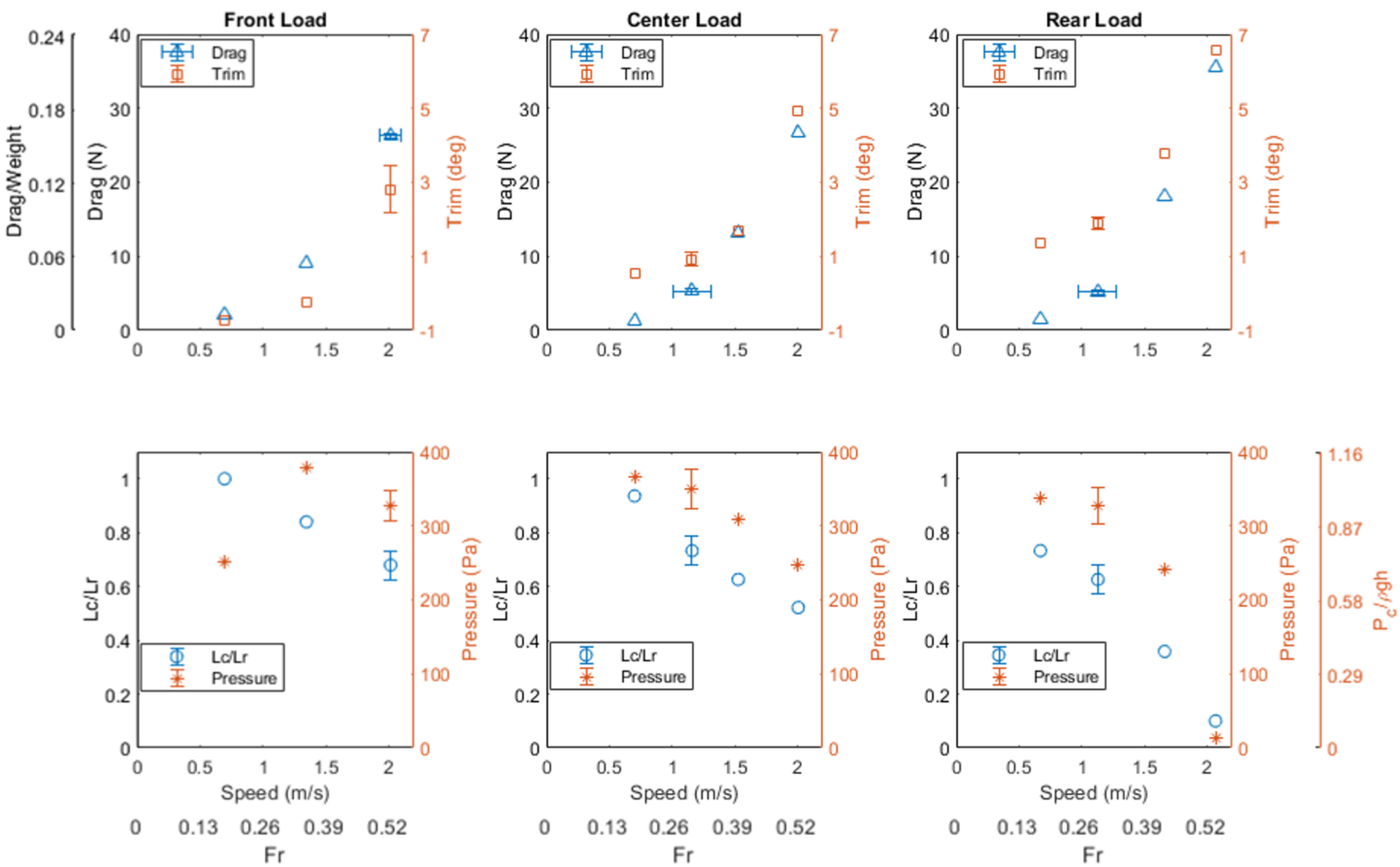

Figure 5. Experimental results for drag, trim, cavity length, and cavity gage pressure for tested speed and loading conditions.

COMPUTATIONAL METHOD

Hydrodynamic simulations of the tested boat were carried out with two degrees of freedom (trim and heave) using CFD software STAR-CCM+ version 15.04. The hull geometry and numerical domain are shown in Figure 7. Water depth was set at 75 cm to approximately match with experimental conditions. The inlet and outlet are positioned 3 m from the bow and stern, respectively, allowing two hull lengths in either direction for flow development. Width of the domain was 80 cm, which is four times larger than the hull beam width.

Slip walls were used on the domain top, bottom and one side boundary. A symmetry plane was imposed on the other side boundary passing through the hull centerplane. A flat volume-of-fluid (VOF) wave was assigned to the constant velocity water inlet, with hydrostatic pressure maintained at the outlet. Water was treated as a constant density fluid and air as an ideal gas, both at a constant temperature of 293 K. The hull surface was a no-slip wall with a roughness height of 0.02 mm for fiberglass and 0.001 mm for acrylic. Solid boundaries were assigned a contact angle of 90°. Air injection was modelled using a constant mass-flow inlet with a half-model flow rate of 0.05 g/s.

Overset meshing approach was used with linear interpolation to map solutions between the stationary background region and the moving region near the solid hull. Assuming flow symmetry about the centerline, a half model was used with refinements added to the free water surface, overset region, hull surface, and cavity recess. Refinement zones are visible along the symmetry plane in Figure 7b,c. Trimmed cells were used for the background and overset regions, with prism layers applied along the main hull. Prism layers were disabled along the recess ceiling in favor of maintaining uniform cell sizes in the cavity refinement.

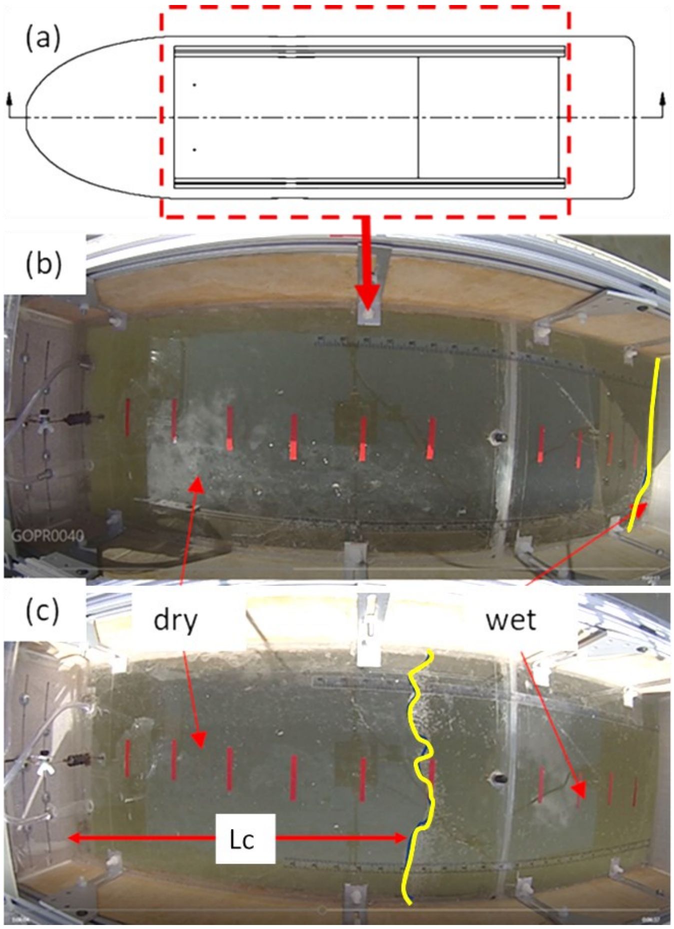

Figure 6. Hull outline with boxed region indicating camera view (a), long cavity (b), short cavity (c). Cavity tail boundary is highlighted in yellow, with corresponding wet and dry regions of the recess ceiling indicated by arrows on either side of the cavity boundary.

Flow was modeled using unsteady RANS equations with 2nd order upwind spatial and 1st order implicit time schemes. The governing continuity and momentum equations are given as follows,

$$\frac{\partial \rho}{\partial t} + \frac{\partial(\rho u_j)}{\partial x_j} = 0 \quad (1)$$

$$\frac{\partial(\rho u_i)}{\partial t} + \frac{\partial(\rho u_i u_j)}{\partial x_j} = -\frac{\partial P}{\partial x_i} + \frac{\partial}{\partial x_j}\left[\mu\left(\frac{\partial u_i}{\partial x_j} + \frac{\partial u_j}{\partial x_i}\right) - \rho\overline{u_i' u_j'}\right] + \rho f_i \quad (2)$$

where ρ is the average density, u is velocity, P is pressure, μ is dynamic viscosity and f represents the volume fraction of a given fluid species. Using the VOF method, average density ρ and viscosity μ are

$$\mu = \beta\mu_{air} + (1-\beta)\mu_{water} \quad (3)$$

$$\rho = \beta\rho_{air} + (1-\beta)\rho_{water} \quad (4)$$

with β representing the air volume fraction.

Turbulence was simulated using the two-layer all-y+ realizable $k-\varepsilon$ model. SST $k-\omega$ and RNG $k-\varepsilon$ were also considered as turbulence models, but hull trim showed weaker agreement with experimental results. Differences in total drag and cavity states were negligible.

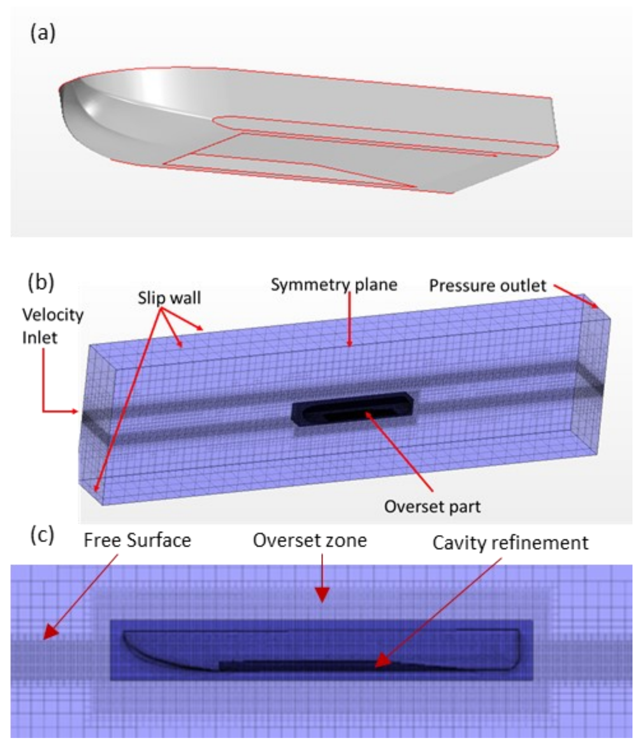

Figure 7. Solid hull geometry (a), computational domain and boundary types (b), side view of mesh refinements (c)

Time steps for each condition were small enough to maintain the average Courant number below 0.5 near the wetted hull surface, with each step resolved by 10 inner iterations. Air-water interactions were modelled with a segregated flow solver using the volume of fluid (VOF) method. As in the experimental method, a large airflow was initially supplied to form the cavity and then reduced to the experimental flow rate to obtain steady state numerical solutions. High resolution interface capturing (HRIC) was applied with a sharpening factor of 0.5 to suppress numerical diffusion of the volume fraction advection term while maintaining a modest overall cell count. Gravity was activated, and surface tension was set to 0.072 N/m.

Free motion was selected for the dynamic fluid-body interaction (DFBI) solver and the half-model was assigned a mass of 8.4 kg. Longitudinal centers of center of gravity (LCG) for each experimental loading were assigned at 4 cm, 10 cm, and 16 cm aft of midship, similar to experimental loadings. The moment of inertia with respect to the transverse axis was assigned a value of 1.5 kg·m^2.

Using the front load condition at U = 1.34 m/s for a validation case, three different mesh levels were applied by reducing the base cell size and near wall prism height by a factor of 1.41. The near wall y+ values were mainly in the range between about 30 and 70. Results are listed in Table 2.

Table 2. Numerical solutions for average cavity length, drag and trim with mesh refinement

Cell count	Lc/Lr	Drag (N)	Trim (°)	Pressure (Pa)
377,885	0.738	4.42	0.259	330.6
973,932	0.779	3.85	0.015	344.0
2,537,098	0.794	3.64	-0.064	347.4

The discretization error ϵ_h for each field variable was found using Richardson extrapolation [25], given by

$$\epsilon_h \approx \frac{\phi_h - \phi_{\sqrt{2}h}}{r^p - 1} \tag{5}$$

where ϕ_h is the solution obtained on grid size h, r is the chosen mesh refinement factor (1.41 in this case), and p is calculated by

$$p = \frac{\log\left(\frac{\phi_{\sqrt{2}h} - \phi_{2h}}{\phi_h - \phi_{\sqrt{2}h}}\right)}{\log r} \tag{6}$$

The numerical errors ϵ_N listed in Table 3 include a safety factor of 1.25, which has been recommended for mesh refinements showing monotonic convergence for three or more grid sizes [26].

Table 3. Numerical uncertainties for calculated metrics

ϕ	ϵ_N
Lc/Lr	0.079
Pressure (Pa)	1.46
Drag (N)	0.145
Trim (°)	0.047

COMPUTATIONAL RESULTS

Numerical solutions are compared with experimental results from the front load condition in Figure 8. Drag values with a steady air cavity were within 16-19% of the experimental average at higher speeds and showed worse relative agreement at low speeds, although drag magnitude is very small at low speeds. Despite showing good agreement with all other metrics, total drag was underpredicted at this condition (Re ≈ 10^6, Fr ≈ 0.18). For all speeds, trim values were within experimental uncertainty.

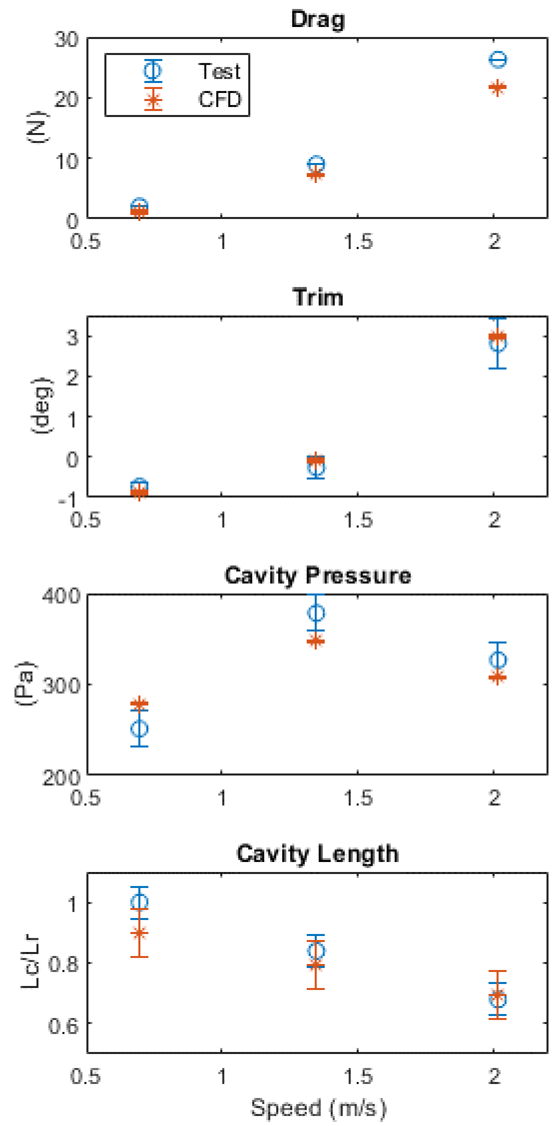

Figure 8. Numerical and test results for the front-loaded hull

Volume fraction images for the air cavity are shown along the symmetry plane in Figure 9. Numerical results for the lowest speed (Figure 9a) affirm the experimental hypothesis that a thinner cavity occurred at this condition, which correlated with lower cavity pressure. At the highest water speed (Figure 9c), the cavity tail became more active in its shedding patterns and failed to obtain smooth reattachment to the beach. Accurately capturing flow physics near the cavity closure is necessary to predict total air leakage, which was the subject of recent computational research by Rotte et al. [27]. While this study did not focus on air leakage or obtain detailed measurements of the cavity closure, the economical computational settings used here were able to qualitatively show changes at different water speeds.

Disturbances on the free water surface were much greater at the highest speed and the downstream wake became visibly larger in amplitude. Since the same mesh settings were used for all cases, the free surface refinement zone was sized to fully enclose the peak of the largest generated wave. Some interface smearing is noticeable on the main water surface which could have been improved with a finer mesh, although cavity interfaces appear to be well resolved.

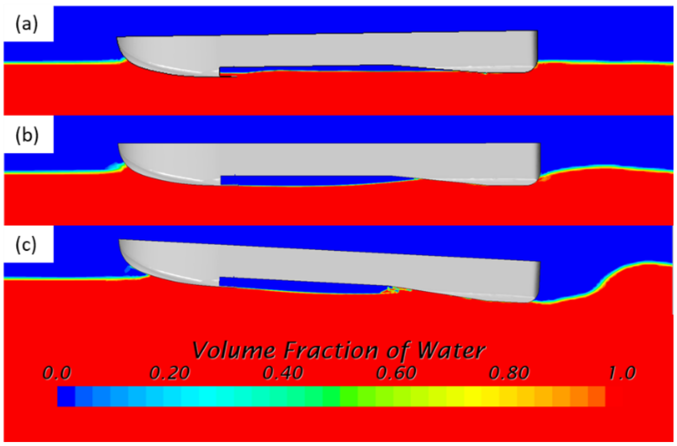

Figure 9. Volume fraction images for U = 0.70 m/s (a), U = 1.34 m/s (b), U = 2.01 m/s (c).

Figure 10 shows the velocity field for each tested speed. In all cases, it can be seen that velocity magnitude is much lower inside of the cavity than in the water flow region. Significant non-uniformity of flow fields inside the cavity become visible at U = 1.34 m/s, and increase at U = 2.01 m/s. Since the air injection rate was constant in all cases, enhanced flow patterns inside the cavity were influenced only by hull trim and water flow properties near the cavity interface. Changes to the incident water velocity are also visible under the bow for the two lower speeds, where some acceleration of the water flow in this region was predicted by the solver.

To investigate possible model improvements, it is necessary to consider both turbulence and meshing strategies. The flow features associated with this hull geometry raise the question of proper turbulence model and near wall cell size, especially at lower speeds where CFD predictions showed poor relative agreement with the experiment. Ships with a bottom air cavity recess experience water flow separation and reattachment along the hull even at slow speeds, which are not explicitly captured using the $k-\varepsilon$ model or wall functions. Low speeds here were also more affected by the transition to turbulence. As mentioned in earlier sections, other turbulence models compatible with this mesh were also applied but showed no significant changes in total drag or cavity state.

As a final numerical test, the adaptive mesh refinement (AMR) and time step controls were activated to explore their suitability for air cavity ship modelling. Since the adaptive controls cannot coarsen cells beyond their initial level, the medium grid from the mesh validation case was chosen as a starting point. Due to limited computational resources and the exploratory nature of this task, two mesh refinement steps were initially allowed for each the free surface and overset region, then disabled for the main flow environment and reduced to only a single refinement step in the overset region. Three user defined functions were also included to refine cells with volume fractions of air between 0.15 and 0.85, and to coarsen cells with volume fractions of air or water greater than 0.995. Isotropic prism layer refinement was enabled, and the number of cells increased from ~1.0 x 10^6 to ~2.9 x 10^6. Compared to the fine mesh obtained by standard refinement, the adaptive mesh added about 10% more cells to the domain with phase interfaces more specifically targeted.

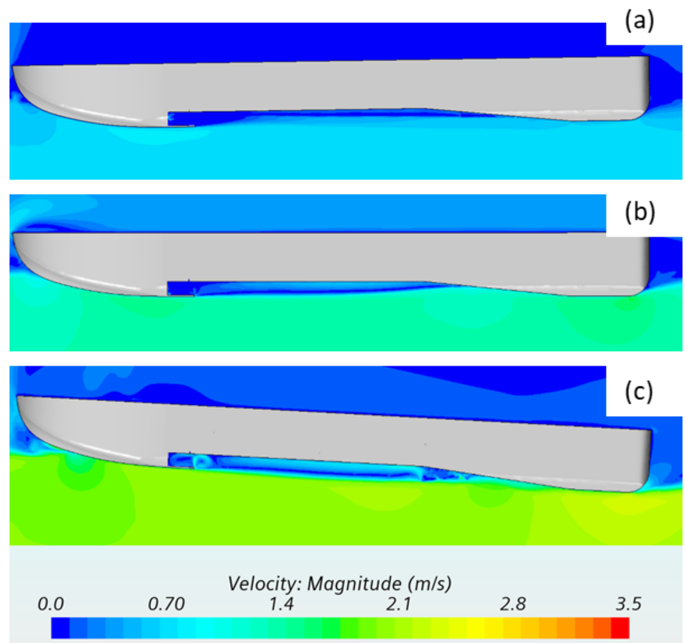

Figure 10. Velocity fields around the air cavity for U = 0.70 m/s (a), U = 1.34 m/s (b), and U = 2.01 m/s (c).

Results obtained on the standard mesh used a time step of 0.002 s to maintain Courant numbers around 0.5 near the wetted hull surface. For the adaptive mesh with very fine cells around phase interfaces, using the same time step caused divergence in the simulation since air leakage was very fast in relation to the fine cell sizes. The adaptive time step criterium in this case was chosen to keep average Courant number for the entire domain around 0.5. This resulted in a time step around 0.00023 s, representing nearly a ten-fold increase in total computational time.

Solutions obtained with standard and adaptive controls are compared in Table 4, along with their respective agreement with experimental values. Cavity length was overpredicted by about 3% of the total recess length using the adaptive mesh, compared to a 5% underprediction by the standard mesh. Computational results for hull trim were within experimental uncertainty for both meshing strategies, although the adaptive mesh predicted slightly more negative trim. This was likely influenced slight differences in the hull pressure distribution between meshes, while the longer air cavity predicted by the adaptive mesh added more lifting force aft of CG. For both cases, total drag and cavity pressure showed negligible changes.

Table 4. Computational results for standard and adaptive meshing. Error is reported in relation to experimental values.

∅	**Standard Mesh**	**Error**	**Adaptive Mesh**	**Error**
Lc/Lr	0.795	-0.045	0.865	0.026
Pressure (Pa)	347.4	-31.0	347.3	-31.1
Drag (N)	7.28	-1.72	7.06	-1.94
Trim (°)	-0.06	0.2	-0.34	-0.08

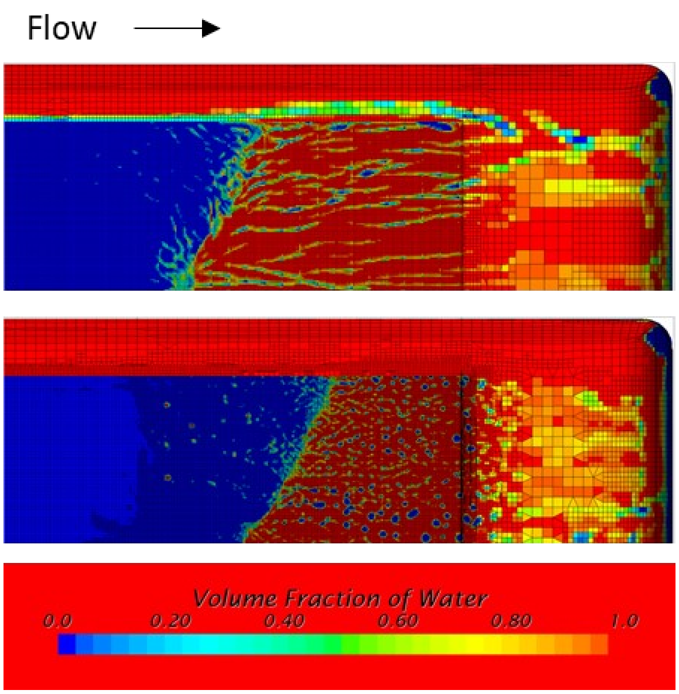

Figure 11. Top view of cavity closure using standard mesh refinement (top) and adaptive mesh refinement (bottom).

Resolution of the cavity closure and shedding patterns were significantly enhanced using the adaptive controls. A top view of the cavity tail is shown with mesh visible for both cases in Figure 11. Compared to the standard mesh with uniform cell sizes in the cavity recess, the adaptive mesh specifically targeted phase interfaces for refinement while leaving cells coarse in the bulk volume of the cavity where enhanced resolution is not needed. This can be advantageous from a design standpoint when the exact cavity closure location is not known in advance, precluding targeted user mesh refinements of these areas during preprocessing.

Downstream of the cavity tail, the size and distribution of air pockets are clearly defined for the adaptive mesh while showing relatively poor resolution on the standard mesh. These fine details of air cavity behavior would be necessary to predict minimum airflow required to sustain the cavity, however, their total impact on hydrodynamic predictions were negligible compared to the tenfold increase in computational power incurred by resolving them.

CONCLUSIONS

An experimental platform was developed to observe important characteristics of an air cavity model hull operating on an open water surface using a remote data acquisition system. Recorded performance metrics were hull trim, total drag, cavity pressure, and cavity length under several speed and loading conditions. Cavity length achieved a maximum with low speeds and slight negative trim, although cavity pressure was decreased under these conditions. Large positive hull trim was detrimental to cavity length and total drag, especially when the recess beach became exposed to incident water flow. Future work on this platform can include alterations to the air cavity recess to improve performance at high speeds and increasing the transmission range of remote signals to accommodate longer run times and distances.

Computational unsteady RANS studies were conducted for selected operating conditions using two degrees of freedom (trim and heave). Cavity length and pressure were generally within 10% of experimental values, while hull trim was within experimental uncertainty for all cases. Drag was underpredicted by 16-19%. Overall, numerical results captured changes in hydrodynamics and cavity states across a variety of water speeds using economical settings for the computational grid and time step. Adaptive mesh and time step controls were activated for one case to compare changes in results with the previously described economical settings. The adaptive controls gave better predictions for total cavity length and significantly enhanced resolution of the cavity tail and shedding patterns, although the required computational time was increased tenfold. Overall predictions for hydrodynamic performance were largely unaffected by the adaptive controls, suggesting that macroscopic behavior of an air cavity hull can be approximately predicted with commercial CFD software using an economical grid size and time step.

ACKNOWLEDGEMENTS

This material is based upon work supported by the National Science Foundation under Grant No. 1800135.

REFERENCES

[1] R. Latorre, "Ship Hull Drag Reduction Using Bottom Air Injection," *Ocean Engineering,* pp. 161-175, 1997.

[2] K. I. Matveev, "Modeling of Vertical Plane Motion of an Air Cavity Ship in Waves," in *5th International Conference on Fast Sea Transportation,* Seattle, USA, 1999.

[3] G. A. Pavlov, L. Yun, A. Bliault and S.-L. He, Air Lubricated and Air Cavity Ships - Development, Design, and Application, New York: Springer, 2020.

[4] K. I. Matveev, "On the limiting parameters of artificial cavitation," *Ocean Engineering,* vol. 30, pp. 1179-1190, 2003.

[5] K. I. Matveev, "Effect of drag-reducing air lubrication on underwater noise radiation from ship hulls," *ASME Journal of Vibration and Acoustics,* vol. 127, no. 4, pp. 420-422, 2005.

[6] B. R. Elbing, E. S. Winkel, K. A. Lay, S. L. Ceccio, D. R. Dowling and M. Perlin, "Bubble-induced skin friction drag reduction and the abrupt transition to air-layer drag reduction," *Journal of Fluid Mechanics,* vol. 612, pp. 201-236, 2008.

[7] S. Makiharju, B. R. Elbing, A. Wiggins, D. R. Dowling, M. Perlin and S. L. Ceccio, "Perturbed Partial Cavity Drag Reduction at High Reynolds Numbers," in *28th Symposium on Naval Hydrodynamics*, Pasadena, 2010.

[8] K. A. Lay, R. Yakushiji, S. Makiharju, M. Perlin and S. L. Ceccio, "Partial Cavity Drag Reduction at High Reynolds Numbers," *Journal of Ship Research,* pp. 109-119, 2010.

[9] A. A. Butuzov, "Artificial cavitation flow behind a slender wedge on the lower surface of a horizontal wall," *Fluid Dynamics,* vol. 2, no. 2, pp. 56-58, 1967.

[10] O. Zverkhovskyi, "Ship drag reduction by air cavities," *Doctoral thesis, Technische Universiteit Delft,* 2014.

[11] R. E. A. Arndt, W. T. Hambleton and E. Kawakami, "Creation and Maintenance of Cavities Under Horizontal Surfaces in Steady and Gust Flows," *Journal of Fluids Engineering,* 2009.

[12] W. Hao, "Numerical study of the effect of ship attitude on the perform of ship with air injection in bottom cavity," *Ocean Engineering,* vol. 186, no. 106119, 2019.

[13] K. I. Matveev, T. J. Burnett and A. E. Ockfen, "Study of air-ventillated cavity under model hull on water surface," *Ocean Engineering,* vol. 36, pp. 930-940, 2009.

[14] J. M. Collins and K. Matveev, "Exploratory Tests of Hydrofoil Influence on Air Cavity under Model Boat Hull," in *Society of Naval Architects and Marine Engineering*, Tacoma, 2019.

[15] A. Shiri, M. Leer-Andersen, R. E. Bensow and J. Norby, "Hydrodynamics of a Displacement Air Cavity Ship," in *29th Symposium on Naval Hydrodynamics*, Gothenburg, 2012.

[16] T. Mukha and R. E. Bensow, "Large-eddy simulation of an internal ship air cavity," in *7th ESI OpenFOAM Conference*, Berlin, Germany, 2019.

[17] G. Rotte, M. Kerkvleit and T. van Terwisga, "On the Turbulence Modelling for an Air Cavity Interface," in *20th Numerical Towng Tank Symposium,* Wageningen, The Netherlands, 2017.

[18] F. Cucinotta, E. Guglielmino, F. Sfravara and C. Strasser, "Numerical and experimental investigation of a planing Air Cavity Ship and its air layer evolution," *Ocean Engineering,* vol. 152, pp. 130-144, 2018.

[19] K. I. Matveev and M. MIller, "Air cavity with variable length under a model hull," *Journal of Engineering for the Maritime Environment,* vol. 225, 2011.

[20] K. I. Matveev and M. V. Pace, "Modification of Air Cavity Flow under Model Hull with Hydrodynamic Actuators," in *Proceedings of the ASME-JSME-KSME Fluids Engineering Conference*, San Francisco, 2019.

[21] A. Day, P. Cameron and E. Nixon, "Moderate-cost approaches for hydrodynamic testing of high performance sailing vessels," in *INNOVSAIL International Conference on Innoavtion in High Performance Sailing Yachts*, Lorient, France, 2017.

[22] K. I. Matveev, "Static Thrust Recovery of PAR Craft on Solid Surfaces," *Journal of fluids and structures,* vol. 24, no. 6, pp. 920-926, 2008.

[23] N. Thompson, P. R. Whitworth, K. I. Matveev, “Development of Small-Scale Unmanned Hydrofoil Boats,” Journal of Unmanned Vehicle Systems, vol. 9, pp. 21-32, 2021.

[24] K. I. Matveev, N. I. Perry, A. W. Mattson and C. S. Chaney, "Development of a Remotely Controlled Testing Platform with Low-drag Air-ventilated Hull," *Journal of Marine Science Applications,* vol. 14, pp. 25-29, 2015.

[25] J. H. Ferziger and M. Peric, Computational Methods for Fluid Dynamics, New York: Springer, 2002.

[26] P. J. Roache, Verification and Validation in Computational Science and Engineering, Albuquerque, NM: Heromosa, 1998.

[27] G. Rotte, M. Kerkvleit and T. van Terwisga, "Exploring the limits of RANS-VoF modelling for air cavity flows," *International Ship Building Progress,* vol. 66, pp. 273-293, 2019.

